

Hybrid diffusion imaging

Yu-Chien Wu^{a,b,c,*} and Andrew L. Alexander^{b,c,d}

^aDepartment of Radiology, University of Wisconsin-Madison, Madison, WI, USA

^bWaisman Laboratory for Brain Imaging and Behavior, University of Wisconsin-Madison, Madison, WI, USA

^cDepartment of Medical Physics, University of Wisconsin-Madison, Madison, WI, USA

^dDepartment of Psychiatry, University of Wisconsin-Madison, Madison, WI, USA

Received 1 October 2006; revised 25 February 2007; accepted 27 February 2007

Available online 24 March 2007

Diffusion measurements in the human central nervous system are complex to characterize and a broad spectrum of methods have been proposed. In this study, a comprehensive diffusion encoding and analysis approach, hybrid diffusion imaging (HYDI), is described. The HYDI encoding scheme is composed of multiple concentric “shells” of constant diffusion weighting, which may be used to characterize the signal behavior with low, moderate and high diffusion weighting. HYDI facilitates the application of multiple data analyses strategies including diffusion tensor imaging (DTI), multi-exponential diffusion measurements, diffusion spectrum imaging (DSI) and *q*-ball imaging (QBI). These different analysis strategies may provide complementary information. DTI measures (mean diffusivity and fractional anisotropy) may be estimated from either data in the inner shells or the entire HYDI data. Fast and slow diffusivities were estimated using a nonlinear least squares bi-exponential fit on geometric means of the HYDI shells. DSI measurements from the entire HYDI data yield empirical model-independent diffusion information and are well-suited for characterizing tissue regions with complex diffusion behavior. DSI measurements were characterized using the zero displacement probability and the mean-squared displacement. The outermost HYDI shell was analyzed using QBI analysis to estimate the orientation distribution function (ODF), which is useful for characterizing the directions of multiple fiber groups within a voxel. In this study, an HYDI encoding scheme with 102 diffusion-weighted measurements was obtained over most of the human cerebrum in under 30 min.

© 2007 Elsevier Inc. All rights reserved.

Introduction

The diffusion tensor is a good model of the diffusion-weighted signal behavior for low levels of diffusion weighting (e.g., $b < 1500$ s/mm²). However, the diffusion tensor model does not appear to be consistently accurate in describing the signal behavior

for higher levels of diffusion weighting. The problems with the simple diffusion tensor model arise from two sources—(1) apparent “fast” and “slow” diffusing components (Niendorf et al., 1996; Mulkern et al., 1999; Assaf and Cohen, 1998a, 2000; Clark and Le Bihan, 2000; Inglis et al., 2001; Ronen et al., 2003; Maier et al., 2004) that cause the signal decay with diffusion weighting to appear non-monoexponential; and (2) partial volume averaging (Alexander et al., 2001) between tissue groups with distinct diffusion tensor properties (e.g., crossing white matter tracts, averaging between white matter and gray matter tissues). The non-monoexponential diffusion behavior is likely to arise from local restriction effects from cellular membranes.

The effect of partial volume averaging causes ambiguities in the interpretation of diffusion tensor measurements. Whereas the diffusion anisotropy is generally assumed to be high in white matter, regions of crossing white matter tracts will have artifactually low diffusion anisotropy. Consequently, in regions with complex white matter organization, changes or differences in diffusion tensor measures may reflect either changes in either the tissue microstructure or the partial volume averaging components. As the diffusion weighting is increased the profiles of apparent diffusivity reveal non-Gaussian diffusion behavior in voxels with partial volume averaging (Niendorf et al., 1996; Mulkern et al., 1999; Assaf and Cohen, 1998a,b, 1999, 2000; Assaf et al., 2000; Clark and Le Bihan, 2000; Alexander et al., 2001, 2002; Frank, 2000). Despite these limitations, the applications of diffusion tensor imaging have been rapidly growing, mainly because of the relative simplicity and good acquisition efficiency (e.g., it can be acquired in clinically acceptable times).

A growing number of strategies have been developed for measuring and interpreting complex diffusion behavior. The methods vary in their acquisition sampling and analysis approaches. High angular resolution diffusion imaging (HARDI) methods (including QBI: *q*-ball imaging; and GDTI: generalized DTI) typically obtain images with a constant moderate to high level of diffusion weighting ($b > 1500$ s/mm²) over a large number (> 30) of non-collinear encoding directions (Liu et al., 2004; Özarslan and Mareci, 2003). The HARDI approaches may be used to detect and characterize regions of crossing white matter tracts;

* Corresponding author. Waisman Laboratory for Brain Imaging and Behavior, Waisman Center, University of Wisconsin-Madison, 1500 Highland Ave., Rm.T231, Madison, WI 53705-2280, USA. Fax: +1 608 262 9440.

E-mail address: yuchienwu@wisc.edu (Y.-C. Wu).

Available online on ScienceDirect (www.sciencedirect.com).

however, they are insufficient for characterizing aspects of non-monoexponential diffusion.

Other methods attempt to bridge the ability to measure both fast and slow diffusion with high angular sampling. The most basic approach is diffusion spectrum imaging (DSI), which obtains diffusion-weighted samples on a Cartesian sampling lattice in q -space (Wedeen et al., 2000, 2005). Diffusion displacement spectra are related to the q -space measurements by a Fourier transform (Callaghan, 1991; Cory and Garroway, 1990; King et al., 1994, 1997; Assaf et al., 2000; Assaf and Cohen, 2000). While Cartesian sampling facilitates the straightforward FFT for estimation of the displacement densities of water molecules, it is not required. Recently, investigators have proposed non-Cartesian sampling strategies of q -space (Assaf et al., 2004; Assaf and Basser, 2005; Wu and Alexander, 2005a,b; Khachaturian et al., 2007). Assaf et al. applied a model (CHARMED) of slow and fast diffusion compartments to estimate what they deemed as hindered and restricted diffusion (Assaf et al., 2004; Assaf and Basser, 2005). In a separate study, we demonstrated that the non-Cartesian q -space sampling strategy that uses concentric spherical shells of constant $|q|$ may be used for estimating DTI, DSI and QBI properties in a single experiment (Wu and Alexander, 2005a,b). The number of encoding directions is increased with each encoding shell to increase the angular resolution with the level of diffusion weighting. Thus, the most interior shells may be used for diffusion tensor analyses where high angular resolution was not essential, and the outermost shell with the highest diffusion weighting and angular resolution may be used for HARDI approach such as QBI analysis. The entire data set from all shells is combined for both DSI and multi-exponential diffusion analyses. This flexible diffusion encoding strategy is called hybrid diffusion imaging (HYDI).

The concentric shell framework used in the HYDI q -space scheme provides flexibility in the data features to be emphasized. DTI works best at lower b values; therefore, the measurements from the inner shells may be used to estimate the diffusion tensor. A minimum of six directions are required to estimate the DT although more may be acquired to improve accuracy. On the outer shell(s) the number of directions may be increased to better characterize complex tissue organization. In this case, QBI may be applied to the outermost shell data. Combining all shells, the whole HYDI data set may be used for DSI. In addition, the behavior of q -space diffusion signals was investigated across all shells, and diffusivities were estimated using both monoexponential and bi-exponential models. The ultimate goal is to develop an efficient diffusion imaging measurement strategy that can provide characterization of complex diffusion in a clinically feasible scan time.

In this paper, a basic demonstration of HYDI is performed using both measured brain image data and simulated data. Strategies for HYDI image analysis are discussed. Finally, a summary and demonstration of several quantitative measures that can be obtained using HYDI are also provided.

Materials and methods

HYDI encoding

The implementation of hybrid diffusion imaging is very similar to diffusion spectrum imaging (DSI) (Wedeen et al., 2005) except that q -space samples are placed on concentric shells instead of a Cartesian lattice. The q -space encoding wave-vector, \mathbf{q} , for a specific HYDI sample using a standard pulsed-gradient spin-echo

pulse sequence is $\mathbf{q} = \gamma \mathbf{G} \delta$, where γ is the gyromagnetic ratio, \mathbf{G} is the encoding gradient vector, and δ is the diffusion-gradient pulse width. The encoding wave-vectors were placed on 5 concentric shells in q -space as listed in Table 1. The total number of q -space encoding samples was 102 including a central $q=0$ sample, and the maximum diffusion weighting corresponded to a b value of 9375 s/mm² (corresponding to a maximum $q=76$ mm⁻¹). On each shell, the samples were arranged uniformly and the number of encoding directions generally increased with the level of diffusion weighting (although the 2nd and 3rd shells both had 12 encoding directions). The specific encoding set is not necessarily optimum from a sampling density or accuracy standpoint, but does adequately illustrate the features of the HYDI encoding strategy. Future studies will be performed to optimize the specific set of encoding directions.

MRI experiments

In vivo brain data with HYDI were obtained on six healthy volunteers using a 3 T GE SIGNA scanner (GE Healthcare, Waukesha, WI). The diffusion weighting (DW) pulse sequence was a single-shot, spin-echo, echo-planar imaging (SS-SE-EPI) pulse sequence with diffusion-gradient pulses, dual-echo gradient refocusing to minimize distortions from eddy currents, and cardiac gating (using a photo-plethysmograph) to minimize signal fluctuation from brain pulsations. The q -space diffusion-encoding scheme is described above. The maximum b value was 9375 s/mm² with a maximum DW gradient of 40 mT/m, gradient duration (δ) and separation (Δ) of 45 and 56 ms, respectively. This sampling scheme corresponded to a shell spacing of $\Delta q_r = 15.2$ mm⁻¹ and a maximum $q=76.0$ mm⁻¹ (Table 1). The field of view (FOV= Δq_r^{-1}) and the resolution ($2\max q_r$)⁻¹ of the displacement density of water molecular are 65 μ m and 6.57 μ m, respectively. Other imaging parameters included an in-plane voxel size=2 mm (FOV=25.6 cm and matrix size=128 \times 128), 30 slices with slice thickness=3 mm covering most of the cerebrum, TE/TR=122/11700 ms and a total scanning time of approximately 30 min. SNRs were calculated for each shell. The signals were the mean diffusion-weighted signals at each shell. The noise was estimated by the standard deviation of the subtraction of two images at $b=0$ s/mm² scaled by a factor of $\sqrt{2}$.

HYDI data processing

The HYDI encoding approach is extremely flexible for a wide spectrum of diffusion image analyses. The acquisition of diffusion-encoded images on shells with constant diffusion weighting is amenable to DTI and QBI analyses. The entire data set may be

Table 1
The HYDI q -space encoding scheme

Shell	Dir. #	Δq_θ (°)	q_r (1/mm)	Δq_r (1/mm)	b value (s/mm ²)
	1				0
1st	3		15.2	15.2	375
2nd	12	48°	30.4	15.2	1500
3rd	12	48°	45.6	15.2	3375
4th	24	42°	60.9	15.2	6000
5th	50	30°	76.0	15.2	9375
Total	102	Mean 40°	Max 76.0	Mean 15.2	Max 9375

regrided to a Cartesian lattice for DSI analysis. These approaches are described here.

At lower levels of diffusion weighting (i.e., $b < 2000 \text{ s/mm}^2$), the diffusion tensor model is generally a good description of the signal behavior. In this study, conventional diffusion tensor image analysis was performed using data from shells with diffusion weighting (DW) up to $b = 1500 \text{ s/mm}^2$ (Table 1, shells 0 to 2). In addition, diffusion tensor maps were also estimated using the entire HYDI data set to match the data and SNR for comparisons between DTI and DSI. The diffusion tensor elements were calculated using nonlinear least squares estimation with the *Camino* software package (Cook et al., 2006). DT measures including the mean diffusivity (MD), the fractional anisotropy (FA) and the major eigenvector color map were derived from the diffusion tensor (Basser and Pierpaoli, 1996).

To evaluate the deviation of the diffusion-weighted signals from an ideal Gaussian distribution (the basis for the diffusion tensor), we calculated the root-mean-square (RMS) of the q -space signal residuals from the fit to the diffusion tensor model. The higher RMS errors reflect larger deviation of the q -space signals from the Gaussian diffusion model.

At higher levels of diffusion weighting, q -ball imaging (QBI) appears to yield relatively high angular resolution (Tuch et al., 2003). Thus, the data in the outermost shell (Table 1—shell 5 with 50 directions at $b = 9375 \text{ s/mm}^2$) were used for QBI analysis. The QBI-ODF (orientation density function) was reconstructed using the Funk–Radon transform (Tuch et al., 2003),

$$\text{ODF}_{\text{QBI}}(\hat{\mathbf{R}}) = \int_{\vec{q} \perp \hat{\mathbf{R}}} E(\vec{q}) d\vec{q} \quad (1)$$

where $\hat{\mathbf{R}}$ is the unit vector of the dynamic displacement and $E(\vec{q})$ is the q -space signal, $E(\vec{q}) = S(\vec{q})/S(0)$. For each direction ($\hat{\mathbf{R}}$), the ODF is the integral of q -space signals on the circle perpendicular to $\hat{\mathbf{R}}$ on the sphere (e.g., equator).

The entire HYDI data set in Table 1 was used for diffusion spectrum imaging (DSI) analyses. First, to minimize overestimation of signals near the noise floor, q -space signals were set to zero if smaller than 2 times of the mean signal in air. Second, non-uniform q -space signals were regridded onto a $9 \times 9 \times 9$ Cartesian lattice using a bilinear interpolation algorithm (MATLAB function

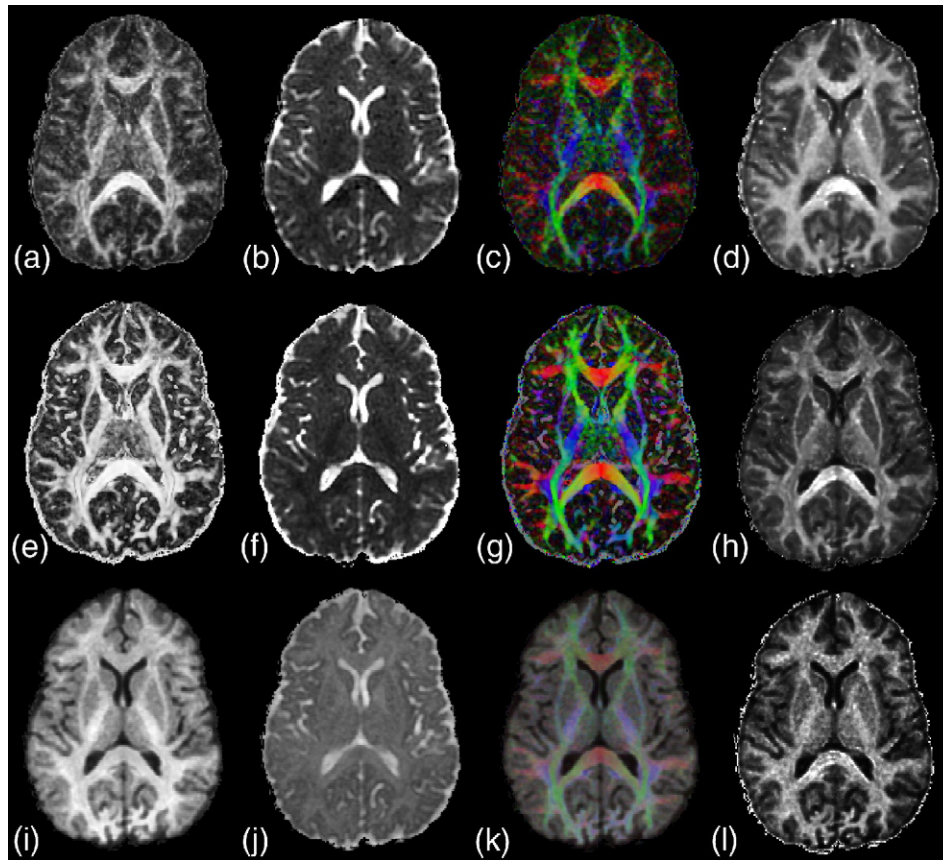


Fig. 1. Quantitative maps from the HYDI MR experiments. DTs calculated from inner the shells and from the entire HYD data set are shown in the upper and middle rows, respectively. Inner shells DT was estimated using a linear least squares fit whereas whole data set DT was estimated using a nonlinear least squares fit. DT measures: FA (a and e), MD (b and f) and major eigenvector color map (c and g). PDF measures, including Po (i), MSD (j) and FWHM color map (k) modulated by Po, were calculated using a DSI reconstruction of the entire HYDI data set. The color codes for both major eigenvector color maps and FWHM color maps is left–right=red, anterior–posterior=green and superior–inferior=blue. The grayscale of (b), (f) and (j) is 0 to $2500 \times 10^{-6} \text{ mm}^2/\text{s}$. The root-mean-square (RMS) of residuals between the DT model and the measured q -space diffusion-weighted signals are in (d) and (h). Higher intensity reflects larger deviation of the DTI model to the real DW signals. (l) The map of the geometric mean of the QBI images ($b = 9375 \text{ s/mm}^2$) normalized by the signal at $b = 0$.

“griddatan”) (Barber et al., 1996). After sample interpolation, the probability density function (PDF) of the water diffusion displacement at the diffusion time Δ was calculated using the Fourier transform (FT) of the normalized q -space signals (Callaghan, 1991; Cory and Garroway, 1990; Assaf et al., 2000, 2002a,b; Wedeen et al., 2000, 2005),

$$\text{PDF}(\vec{R}, \Delta) = \text{FT}[E_{\Delta}(\vec{q})] \quad (2)$$

where \vec{R} is the displacement vector of water molecules.

Several measures were derived from the DSI-PDF. The zero displacement probability

$$P_0 = P(\vec{R} = 0, \Delta) \quad (3)$$

describes the probability density of water molecules that minimally diffuse within the diffusion time Δ (Assaf et al., 2000; Wu and Alexander, 2005a,b). The mean-squared displacement (MSD) is defined as (Wu, 2006)

$$\text{MSD} = \iiint \text{PDF}(\vec{R}, \Delta) \cdot \vec{R}^2 d^3 \vec{R} \quad (4)$$

which describes the average diffusivity within a voxel. The Einstein diffusion equation, $\langle \vec{R}^2 \rangle = 6\Delta\bar{D}$, describes a linear relation between the expectation value of \vec{R}^2 and the mean diffusivity. A directional color map is created from measurements of the full-width at half-maximum, $\text{FWHM}_{x,y,z}$, of the PDF in three orthogonal directions (Wu and Alexander, 2005a,b). The q -space measures P_0 and MSD were first described by Assaf et al. in their one-dimensional q -space measurements (Assaf et al., 2000, 2002a,b). In this study, the definition of P_0 was extended to a three-

dimensional calculation. The definition of the “mean displacement”, however, was slightly different as they calculated the mean displacement using the FWHM described in the paper by Cory and Garroway (1990).

The orientation distribution function (ODF) may also be estimated from the entire q -space data by the radial integral of the PDF (Tuch et al., 2003; Wedeen et al., 2000),

$$\text{ODF}(\hat{R}) = \int_{\hat{R}} \text{PDF}(\rho\hat{R}, \Delta) d\rho \quad (5)$$

where $\rho\hat{R} = \vec{R}$. Note that this definition is different than the ODF estimated from the QBI analysis in Eq. (1).

To compare PDF measures and DTI measures in specific tissues, brain segmentation and anatomically specific ROIs were generated for all six subjects. The P_0 map was used for brain tissue segmentation, which used FMRIB’s automated segmentation tool (FAST) software (Zhang et al., 2001). This approach generated plausible tissue segmentation maps of gray matter and white matter. In addition, hand-generated (polygon shaped) regions-of-interest (ROIs) were created for six WM regions and three deep brain GM regions. The WM ROIs included the corpus callosum splenium (CCs), corpus callosum genu (CCg), posterior limb of internal capsule (PLIC), prefrontal WM (WMpf), occipital WM (WMocc) and centrum semiovale (CS), and the GM ROIs included the thalamus (Th), caudate nuclei (Cau) and putamen (Put). The mean and standard deviations of P_0 , FA and MD for both DTI and DSI analysis were computed for the entire WM segmented region and all of the WM and GM subregions.

The multiple-shell acquisition of HYDI also facilitates the calculation of both the arithmetic and the geometric means of diffusion signals for specific levels diffusion weighting ($|q|$).

Table 2

ROI studies of restriction measure (P_0), anisotropy measures (FA from both inner shells and all shells) and mean diffusivity measures (MSD and MD) across six subjects

ROI		P_0	FA Inner shells	FA All shells	MD=MSD/6 Δ (10^{-6} mm ² /s)	MD (10^{-6} mm ² /s) Inner shells	MD (10^{-6} mm ² /s) All shells
CCS		0.113 \pm 0.010	0.857 \pm 0.104	0.922 \pm 0.046	710 \pm 33	652 \pm 141	544 \pm 157
	CV	0.087	0.121	0.050	0.046	0.227	0.290
CCG		0.099 \pm 0.010	0.754 \pm 0.143	0.909 \pm 0.055	734 \pm 43	820 \pm 218	805 \pm 357
	CV	0.103	0.190	0.060	0.058	0.266	0.442
PLIC		0.126 \pm 0.009	0.694 \pm 0.118	0.811 \pm 0.079	696 \pm 29	637 \pm 81	479 \pm 85
	CV	0.074	0.169	0.097	0.042	0.126	0.177
WMpre		0.108 \pm 0.012	0.479 \pm 0.152	0.688 \pm 0.140	723 \pm 28	714 \pm 114	609 \pm 149
	CV	0.107	0.318	0.203	0.039	0.160	0.245
WMocci		0.121 \pm 0.011	0.559 \pm 0.141	0.755 \pm 0.113	704 \pm 27	661 \pm 102	527 \pm 124
	CV	0.088	0.252	0.149	0.039	0.154	0.237
CeSe		0.121 \pm 0.013	0.482 \pm 0.141	0.695 \pm 0.145	704 \pm 29	660 \pm 87	518 \pm 104
	CV	0.111	0.293	0.209	0.041	0.133	0.200
Thalamus		0.088 \pm 0.014	0.439 \pm 0.136	0.518 \pm 0.131	710 \pm 42	745 \pm 177	710 \pm 325
	CV	0.160	0.310	0.252	0.059	0.238	0.459
Caudate		0.072 \pm 0.009	0.361 \pm 0.163	0.363 \pm 0.161	702 \pm 41	750 \pm 142	744 \pm 148
	CV	0.120	0.450	0.444	0.058	0.189	0.199
Putamen		0.076 \pm 0.008	0.382 \pm 0.148	0.363 \pm 0.136	711 \pm 41	693 \pm 139	604 \pm 156
	CV	0.102	0.388	0.374	0.058	0.200	0.225

Abbreviations for ROI: CCS: corpus callosum splenium; CCG: corpus callosum genu; PLIC: posterior limb of internal capsule; WMpre: prefrontal white matter; WMocci: occipital white matter; CeSe: centrum semiovale.

The error denotes one standard deviation across six subjects and ROI.

CV denotes the coefficient of variation, which is defined as the ratio of the standard deviation to the mean value.

Means of the diffusion-weighted signals were then used to estimate mean diffusivities. Since the diffusion is not expected to be monoexponential over the entire range, two strategies were implemented for characterizing the diffusivities. The first was to estimate the mean apparent diffusivities over small ranges of b values. In this case, monoexponential diffusion was estimated for different shell sub-ranges of the mean q -space signals — i.e., $b=0$ to 1500 s/mm^2 (shells 0, 1, 2); $b=375$ – 3375 s/mm^2 (shells 1, 2, 3); $b=1500$ – 6000 s/mm^2 (shells 2, 3, 4); and $b=3375$ – 9375 s/mm^2 (shells 3, 4, 5). Obviously, the data in the higher b value ranges will emphasize the slow diffusion components and the low b value ranges the faster diffusion components. This was done for both the geometric and arithmetic means.

In the second approach, the geometric means, GM_s , across all shells, s , were fitted to a one-dimensional bi-exponential model using a nonlinear least squares algorithm. The bi-exponential model is described as

$$GM_s = f_1 \exp(-D_1 \cdot b_s) + f_2 \exp(-D_2 \cdot b_s) + \text{const.} + \text{noise.} \quad (6)$$

where f_1 and f_2 are the volume fractions, D_1 is the assumed fast diffusivity, D_2 is the assumed slow diffusivity, and const. is constant. This model has one constraint, i.e., $f_1 + f_2 = 1$, and 4 variables (f_1 , D_1 , D_2 and constant) needed to be estimated. The HYDI acquisition has 6 shell sample points (including measurements at $b=0$) that were used for the estimation.

Computer simulation

To study the ODF angular errors and angular resolution of the HYDI encoding scheme, a Monte Carlo noise simulation was performed. Both fast and slow diffusion compartments (Clark and Le Bihan, 2000; Maier et al., 2004) were simulated for each tract group, including for crossing white matter tracts. Diffusion measurements in corpus callosum were used to simulate fast and slow Gaussian diffusion functions (Maier et al., 2004). The q -space signal was modeled using

$$S(\vec{q}) = S(0) \sum_{i=1}^n [f_{if} \exp(-\vec{q} D_{if} \vec{q}') + f_{is} \exp(-\vec{q} D_{is} \vec{q}')] \quad (7)$$

where n was the total simulated fiber number, f_{if} was the volume fraction of the fast component of the i th fiber, and f_{is} was the volume fraction of the slow component. The summation of all volume fractions was 1, i.e., $\sum_{i=1}^n f_{if} + f_{is} = 1$. D_{if} and D_{is} described the diffusion tensor for both fast and slow component of the i th fiber assuming no exchange between compartments. Gaussian random noise was added the q -space signals in quadrature (Pierpaoli and Bassar, 1996). The magnitude of noised signals was used for data processing. The SNR was calculated as the ratio of the zero DW signal to the standard deviation of the Gaussian noise. Six SNR levels (i.e., 10, 20, 30, 40, 50 and 100) were studied, and for each SNR level, 100 random trials were

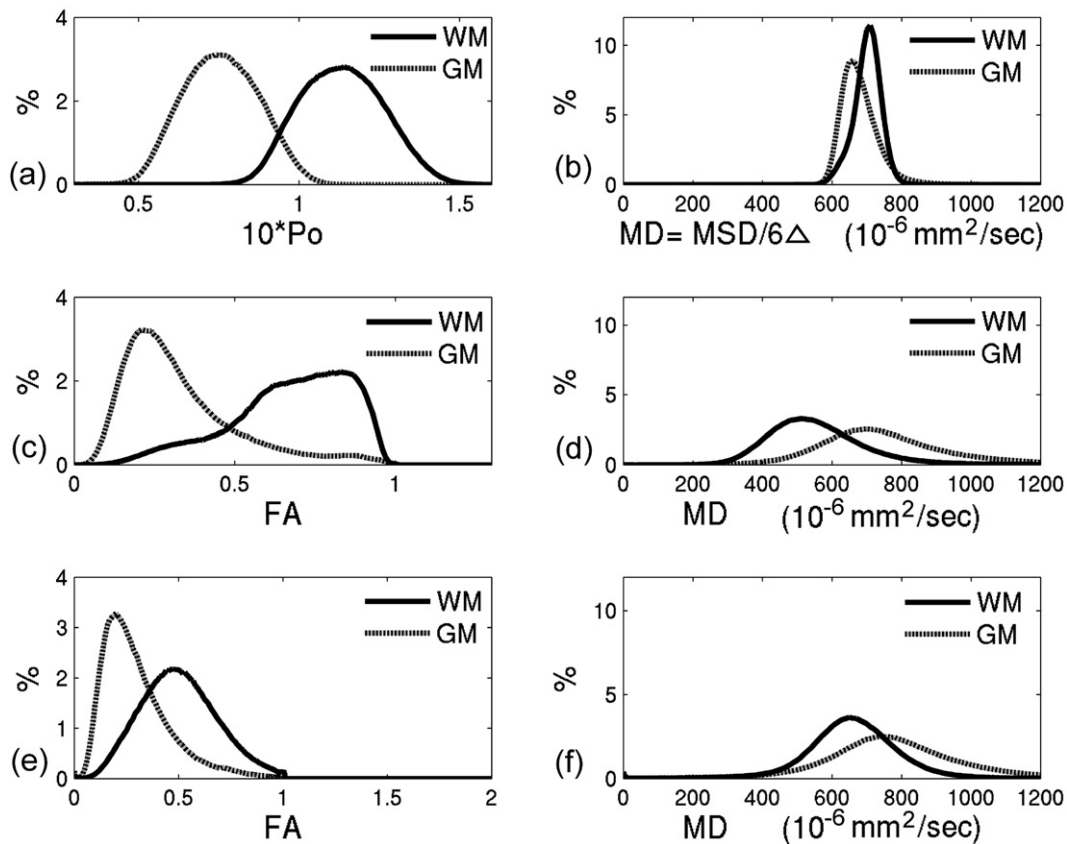


Fig. 2. Histograms of PDF and DT measures for whole brain WM and GM. PDF measures: (a) Po and (b) MSD. DT measures from entire HYDI data: (c) FA and (d) MD. DT measures from inner shells: (e) FA and (f) MD. WM and GM were selected by using FAST segmentation on Po maps. The histograms were generated from the combined results of six subjects.

Table 3

Statistical summary of restriction measure (Po), anisotropy measures (FA from both inner shells and all shells) and mean diffusivity measures (MSD and MD) for both WM and GM, which were segmented by FAST on Po maps of six subjects

		Po	FA Inner shells	FA All shells	MD=MSD/6Δ (10 ⁻⁶ mm ² /s)	MD (10 ⁻⁶ mm ² /s) Inner shells	MD (10 ⁻⁶ mm ² /s) All shells
WM		0.113±0.013	0.505±0.182	0.671±0.183	701±39	660±140	564±191
	CV	0.114	0.360	0.273	0.056	0.212	0.339
GM		0.076±0.012	0.299±0.164	0.329±0.180	679±52	778±216	799±360
	CV	0.155	0.548	0.548	0.077	0.278	0.451

The error denotes one standard deviation across six subjects and whole brain GM/WM.

CV denotes the coefficient of variation, which is defined as the ratio of the standard deviation to the mean value.

simulated to study ODF angular error and ODF angular resolution, respectively.

For the investigation of errors in the estimated fiber direction, a single-fiber (i.e., $n=1$) WM model was used. We generated 100 uniform tensor orientations over one hemisphere using an analytical approach (Hasan et al., 2001; Wong and Roos, 1994). The angular error was defined as the angular differences between the ideal direction and the direction of the maximum likelihood of the ODF profile which is obtained from either the QBI (outermost shell) or DSI (all shells) analyses (Campbell et al., 2004, 2005). For the investigation of the ODF angular resolution, a WM model of two-crossing fibers (i.e., $n=2$) was used. Four intersection angles (45°, 60°, 75° and 90°) and 100 random trials for each intersection angle were simulated. The ODF angular resolution is defined as the average number of fibers that can be separated from the ODF profile of the crossing-fiber configuration among the 100 random trials.

Results

Maps of diffusion tensor (DT) measures calculated from HYDI inner shells are shown in Figs. 1(a)–(c). Maps of DT measures calculated from the entire HYDI data set are shown in Figs. 1(e)–(g). PDF measures from DSI analysis are in Figs. 1(i)–(k). There are some similarities between the contrast in FA and Po maps (Figs. 1(a), (e) and (i)), MD and MSD (Figs. 1(b), (f) and (j)), and the eigenvector and FWHM color maps (Figs. 1(c), (g) and (k)). However, one difference between FA and Po appeared at the fiber crossing areas, such as the prefrontal and occipital WM, the Po map (Fig. 1(i)) demonstrated a more uniform intensity in WM than the FA maps (Figs. 1(a) and (e)). This observation was further supported by an ROI study across 6 subjects (Table 2). For single-fiber ROIs including the corpus callosum splenium (CCs), corpus callosum genu (CCG) and posterior limb of internal capsule (PLIC), FA values of the whole data set (Table 2, column 4) were larger than 0.8 with the coefficient of va-

riation (CV) of ~5–10%. However, for the complex WM ROIs including prefrontal WM (WMpre), occipital WM (WMocci) and centrum semiovale (CeSe), mean FA (all shells) values decreased to ~0.7 with increased CV of 15–20%. In contrast, Po values (Table 2, column 2) are more consistent (~0.10–0.12) between homogeneous and heterogeneous WM ROIs with similar CVs of roughly 10%. In general, WM FA values from the inner shells (Table 2, column 3) were smaller and more heterogeneous (0.48–0.86) than that from the whole data set (Table 2, column 4) with larger CVs (12–32%), whereas GM FA values (0.36–0.52) and their CVs (25–45%) were very similar in both data sets.

Maps of Po also showed that WM (mean±SD=0.115±0.010) including complex regions appeared consistently separable from deep brain GM (~0.0786±0.010). Whole brain segmentation was performed on the Po maps using FMRIB's automated segmentation tool (FAST) software (Zhang et al., 2001). The segmented regions were used to construct histograms of estimated Po, FA and MD measures for regions of GM and WM (Fig. 2). The statistics of these distributions are listed in Table 3. It is clear that the histogram overlap between GM and WM is much less for Po than FA. This is primarily because FA in WM is very heterogeneous. The MD distribution estimated from the DSI analysis is also much narrower than the MD estimates from the DTI analyses. However, the distributions for both GM and WM are highly overlapping in all cases, although the relative peak positions are reversed for DSI and DTI analyses.

The WM and GM SNRs for each shell are listed in Table 4. These data were from one subject, and the results were similar in other subjects. The SNR decreased as the b value increased. At the outermost shell ($b=9375$ s/mm²), the WM had mean and peak signals of 13% and 30% of the $b=0$ signal, respectively; and the GM had mean and peak signals of 5% and 16%, respectively.

To investigate the consistency between the estimated diffusion tensor model and the measured q -space signals in the HYDI data, maps of the root-mean-square difference between the DT model

Table 4

WM and GM SNRs of each shell

Shell	0	1st	2nd	3rd	4th	5th
b value (s/mm ²)	0	375	1500	3375	6000	9375
WM SNR	22.65±5.92	17.67±4.13	9.01±2.00	5.02±1.20	3.57±0.90	2.85±0.71
GM SNR	29.33±11.25	21.26±6.38	9.09±2.40	3.38±0.82	1.88±0.44	1.58±0.32

Whole brain WM and GM were segmented by input Po map to FAST algorithm. The standard deviation was calculated across whole brain ROI.

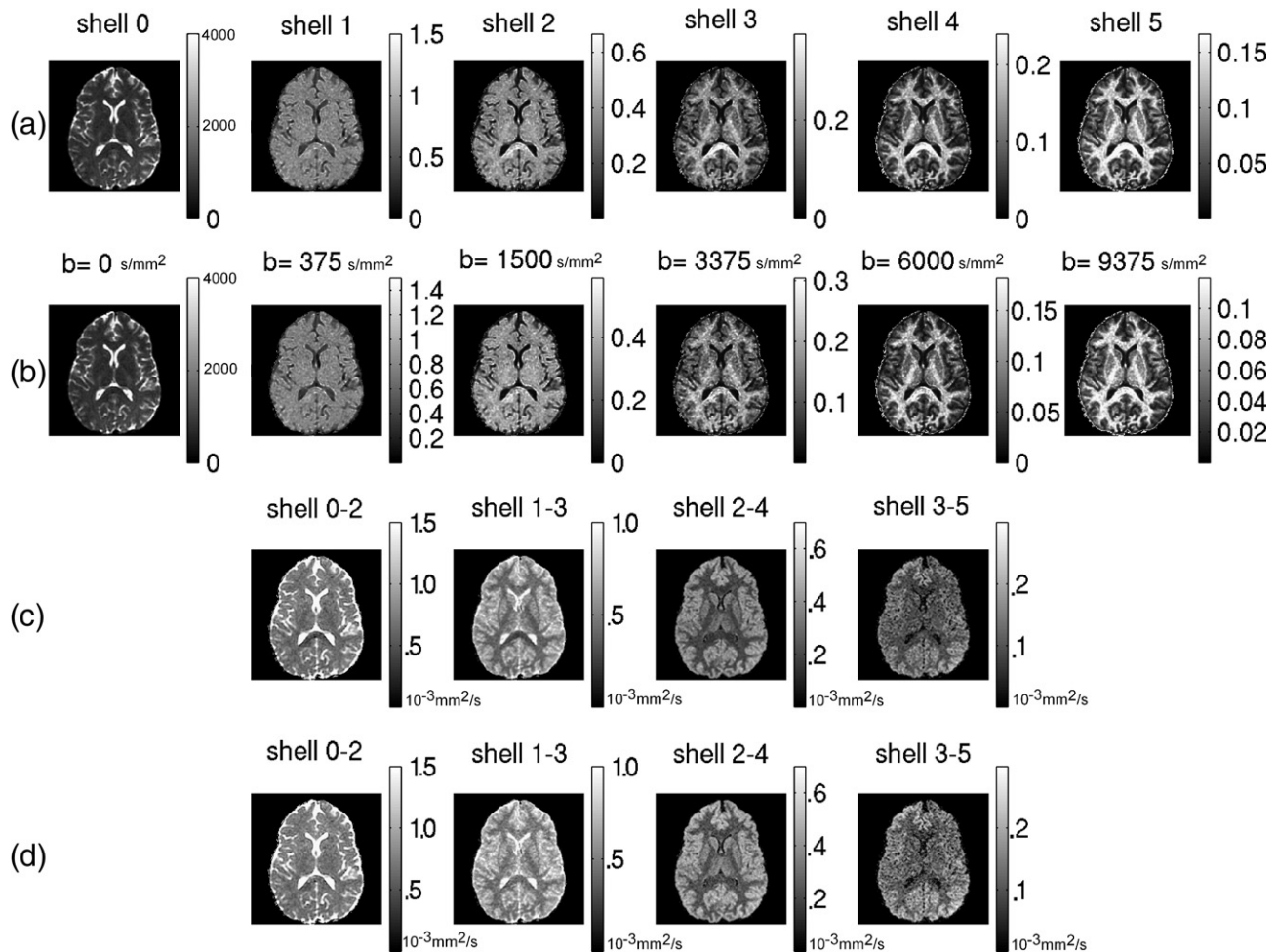


Fig. 3. Mean diffusion signal maps and diffusivity maps at each shell. (a) The arithmetic means. (b) The geometric means. (c) Shell diffusivities estimated from arithmetic means of three contiguous shells. (d) Shell diffusivities estimated from geometric means of three contiguous shells. Diffusivities were estimated using a linear least squares fit with a monoexponential model.

and the q -space DW signals were generated and are shown in Figs. 1(d) and (h). The non-zero intensities in WM indicated the inadequacy of the DT model for describing diffusion signals at high levels of diffusion weighting. The model errors were considerably higher in WM than GM (particularly cortical GM)

where the RMS residuals are close to zero. These results were consistent with the measurement of DT Kurtosis by Jensen et al. (2005) and Lu et al. (2006). A similar map was generated by taking geometric mean of the QBI images normalized by the signal at $b=0$ (see Fig. 1(l)). Again, the signal in WM was

Table 5
Means of diffusion signals and diffusivities at each shell

	Shell	0	1	2	3	4	5
WM	b value (s/mm^2)	0	375	1500	3375	6000	9375
	Arithmetic mean	742 ± 197	587 ± 96	301 ± 58	169 ± 40	121 ± 33	97 ± 27
	Geometric mean	742 ± 197	583 ± 95	282 ± 57	142 ± 37	93 ± 27	72 ± 21
	Da ($10^{-6} \text{ mm}^2/\text{s}$)		609 ± 100	410 ± 63	203 ± 49	93 ± 29	
	Dg ($10^{-6} \text{ mm}^2/\text{s}$)		656 ± 110	468 ± 76	246 ± 58	113 ± 41	
GM	Arithmetic mean	962 ± 373	727 ± 171	317 ± 95	122 ± 47	70 ± 36	60 ± 32
	Geometric mean	962 ± 373	723 ± 170	307 ± 94	103 ± 42	53 ± 28	44 ± 24
	Da ($10^{-6} \text{ mm}^2/\text{s}$)		760 ± 153	600 ± 92	341 ± 78	122 ± 44	
	Dg ($10^{-6} \text{ mm}^2/\text{s}$)		785 ± 161	657 ± 104	396 ± 89	143 ± 57	

Da: the diffusivity calculated using a linear least squares fit of a monoexponential model on arithmetic means of three contiguous shells, i.e., shell 0–2, 1–3, 2–4 and 3–5.

Dg: the diffusivity calculated using geometric means of three contiguous shells.

Whole brain WM and GM were segmented using Po map and FAST algorithm. The standard deviation is across whole brain ROI of one subject.

hyperintense from the restricted diffusion signals. It should be noted that the RMS residuals map for the inner shell DTI data appeared more homogeneous (Fig. 1(d)) than the RMS residuals map for the DTI from the entire data (Fig. 1(h)), particularly in regions of crossing WM.

The HYDI acquisition scheme of spherically symmetric shell of constant q -space radii facilitated the estimation of diffusivities over different diffusion weighting ranges. In this study, both the arithmetic and geometric means were computed for q -space signals at different shells as shown in Figs. 3(a) and (b), and the regional statistics for whole brain WM and GM are listed in Table 5. The tissue contrast between GM and WM appeared to increase with the level of diffusion weighting. The image contrast for both the geometric and arithmetic mean maps was similar although the arithmetic mean signal was consistently higher and appears less noisy, particularly at higher levels of diffusion weighting.

Maps of estimated diffusivities over ranges of three contiguous q -space shells using a linear least squares fit of a monoexponential model are shown in Figs. 3(c) and (d) for both the arithmetic and geometric means, respectively. Mean diffusivity measurements over ranges of $|q|$ for WM and GM are summarized in Table 5. The mean diffusivities decreased as the diffusion weighting was increased. This observation indicated that the diffusion over the entire range of b values was not monoexponential. At high diffusion weighting, the estimated diffusivities of WM were much lower than that in GM. However, for the highest range of diffusion weighting (shells 3–5: $b=3375$ – 9375 s/mm²) the MD maps appear quite noisy.

Fig. 4 and Table 6 summarize the results from bi-exponential fitting (Eq. (6)) of the geometric mean data. The results demonstrated similar fast diffusion signal fractions ($f_1=74\%$) and

Table 6

Results of a nonlinear fit of a bi-exponential model on shell geometric means

	f_1	f_2	D_1 (10^{-6} mm ² /s)	D_2 (10^{-6} mm ² /s)
WM	0.74 ± 0.14	0.26 ± 0.14	996 ± 355	144 ± 116
GM	0.74 ± 0.16	0.26 ± 0.16	1067 ± 447	377 ± 176

Whole brain WM and GM were segmented using Po map and FAST algorithm. f_1 and f_2 are volume fractions for fast diffusivity, D_1 , and slow diffusivity, D_2 , respectively. The standard deviation is across whole brain ROI of one subject.

fast mean diffusivities ($D_1 \sim 1000 \times 10^{-6}$ mm²/s) for GM and WM. However, the slow mean diffusion component for WM ($D_2 \sim 144 \times 10^{-6}$ mm²/s) was slower than GM ($\sim 377 \times 10^{-6}$ mm²/s), which was consistent with the higher levels of restricted diffusion in WM. The fast diffusion component of the mean CSF signals was $>99\%$.

The organization of WM fiber tracts was visualized using ODF profiles generated from QBI analyses using the 50 directional data points in the outer shell of the HYDI encoding. Fig. 5 illustrates examples at the level of the pons (a) and the centrum semiovale (b). In Fig. 5(a) the fiber tract organization in the pontine region revealed corticospinal tracts (blue), central tegmental tract (blue), transverse pontine fibers (red) and the middle cerebellar peduncle fibers (green). In Fig. 5(b), the fibers of the cingulum (green), corona radiata (blue), transverse fibers of corpus callosum (red) and the subcortical arcuate fibers (red) were visualized. These ODF profiles illustrated regions of crossing fibers between these fiber groups at the sub-voxel level.

Simulation results of the ODF angular error versus SNR for both HYDI (DSI analysis) and QBI (outer shell only) are

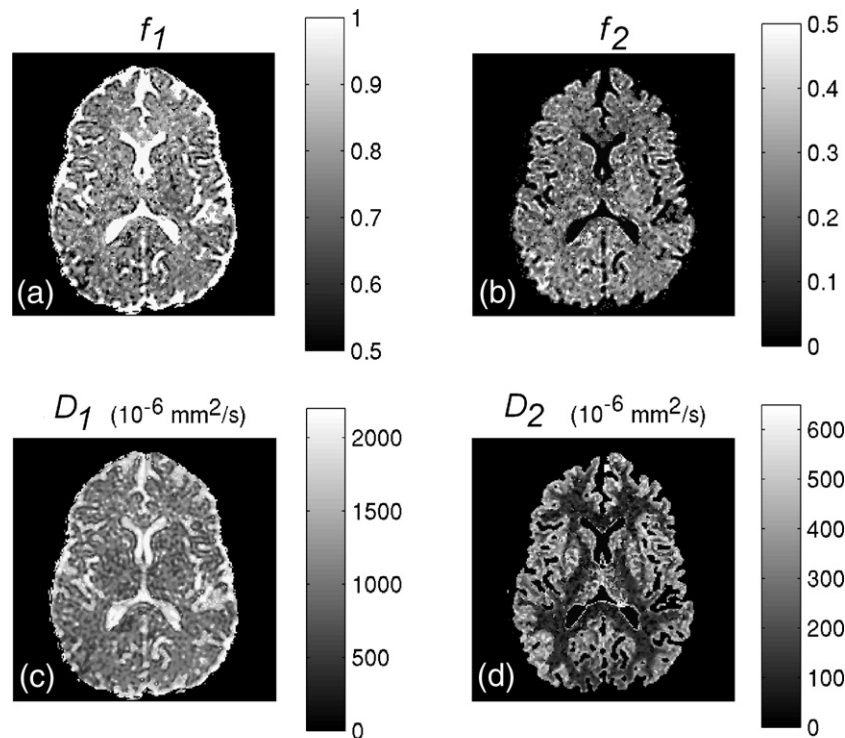


Fig. 4. Results of a nonlinear least squares fit of a bi-exponential model (Eq. (6)) on geometric means in Fig. 3(b). (a) The volume fraction of D_1 . (b) The volume fraction of D_2 . Note that $(f_1 + f_2)$ was assumed to be 1 in this study. (c) The assumed fast diffusivity, D_1 . (d) The assumed slow diffusivity, D_2 .

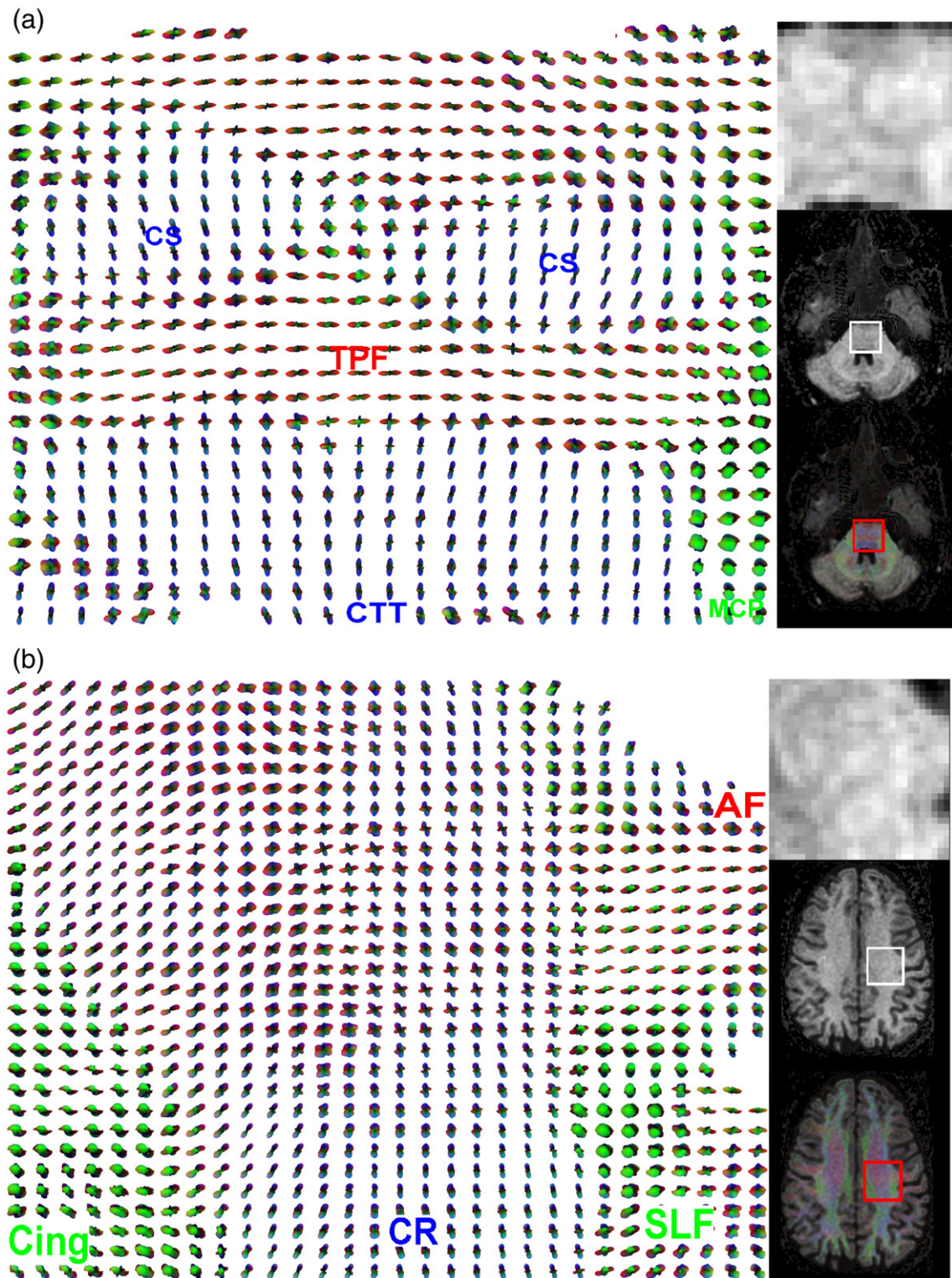


Fig. 5. ODF profiles generated using the QBI algorithm on the outermost shell of HYDI. The regions of interest (ROI) were located at (a) the pons and (b) the centrum semiovale. In general, QBI-ODF has higher angular resolution to resolve multiple crossing fibers. Abbreviation: AF: subcortical arcuate fibers, Cing: cingulum fibers, CR: corona radiata, CS: cortical spinal tract, CTT: central tegmental tract, MCP: middle cerebellar peduncle, SLF: superior longitudinal fasciculus, TPF: transverse pontine fibers.

summarized in Fig. 6. For $\text{SNR} \geq 20$ ($b=0$ data), the angular error was less than 5° for both approaches. Simulated noise-free ODF profiles for crossing WM fibers at different angles are shown in (a).

The influence of noise on the detection of multiple fibers was evaluated and is summarized in Fig. 7(b). The results were relatively insensitive to the SNR level. For a 90° intersection angle,

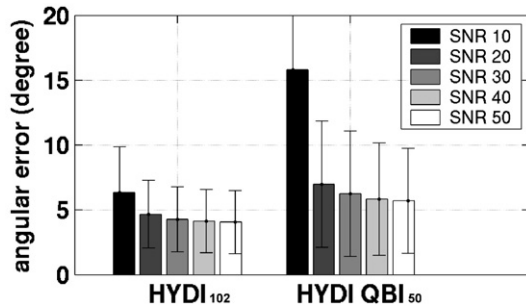


Fig. 6. Estimated angular errors of a single-fiber ODF. The angular error denotes the angular difference between the ideal fiber direction and the direction of the maximum likelihood of ODF profile. The error bar denotes one standard deviation across total 1000 trials (i.e., 10 random trials times 100 directions). The maximum b value for all schemes is 10,000 s/mm².

both methods reliably detected two fibers groups. At 75° and 60° intersection angles, QBI was slightly superior in detecting two fiber groups. At 45°, both methods consistently detected only a single-fiber group. The ability to detect multiple fibers was reduced when the maximum b value was decreased (results not shown).

Discussion

In this study an alternative q -space encoding scheme, HYDI, was described. It was an efficient diffusion imaging approach that was flexible for a wide range of image analysis strategies from a single data set. To our knowledge, this was the first demonstration of simultaneous DTI, DSI, QBI and bi-exponential diffusion analysis from a single diffusion-weighted data set. Possibly, the most similar experimental design is the CHARMED method (Assaf et al., 2004; Assaf and Basser, 2005), which has a similar q -space sampling scheme of concentric q -space shells. From the CHARMED analysis, one may estimate a single hindered (fast) diffusion tensor component and multiple restricted (slow) diffusion components. Thus, the CHARMED method provides information similar to the diffusion tensor, fast/slow diffusion and complex WM organization in a single acquisition. However, the CHARMED method is based upon specific models of diffusion; thus, the results depend heavily on the assumed model. The proposed HYDI framework did not assume any underlying models for most of the analyses – DSI and QBI – and for other analyses it used simpler models for the data – the diffusion tensor and bi-exponential diffusion decay. As the data were acquired using similar schemes, it may be possible to perform CHARMED analysis on HYDI studies. Future studies are necessary to compare HYDI and CHARMED methods more directly.

In a comparison of DSI and DTI measures, the DSI Po and MD indices appeared to be more homogenous and consistent than the DTI FA and MD measures in WM areas. DTI has been shown to be

highly sensitive to averaging between two or more white matter fiber groups in a voxel (Alexander et al., 2001). Conversely, the Po map was sensitive to the most restricted diffusion component of the distribution, which was relatively independent of multiple fiber

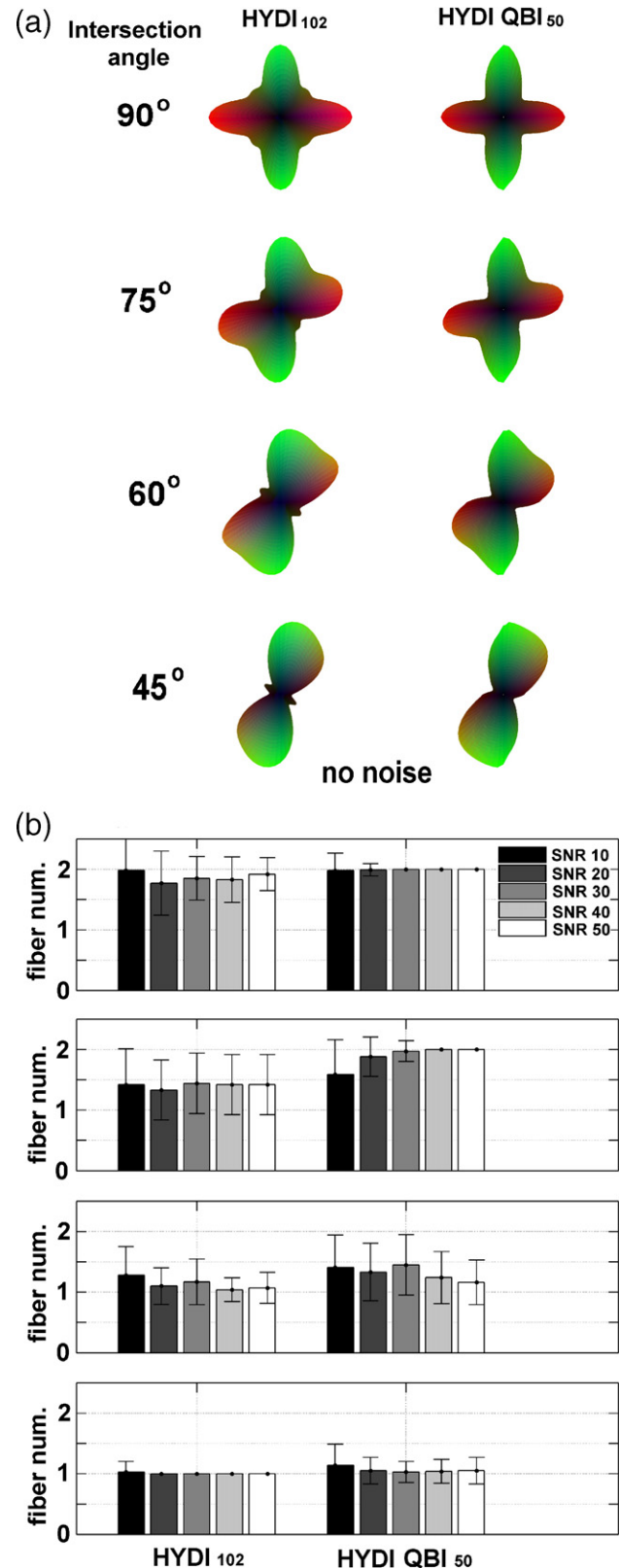


Fig. 7. ODF angular resolution. (a) Simulated noise-free ODF profiles of two crossing fibers with four different intersection angles from 90° to 45°. Two methods were compared including DSI processing on HYDI whole data set, HYDI₁₀₂, and QBI processing on the outermost shell of HYDI, HYDI-QBI₅₀. (b) The average fiber number detected using ODF profiles. The bar plot denotes the mean and standard deviation across 100 trials of random noise on q -space diffusion-weighted signals. The plots from top to bottom correspond to 90°, 75°, 60° and 45°.

groups. In addition the MD estimated from the DSI PDF appeared to have narrower distributions in comparison with the MD measurements from DTI. Obviously, there were challenges associated with comparing DSI and DTI measures as much more data were required for DSI analysis. Consequently, the DTI analysis was performed using two different partitions of the data — the inner shells (0–2) and the entire HYDI data set. The inner shell DTI analysis was more comparable to many published DTI studies although the TE is quite long causing the SNR to be suboptimal. The DTI analysis of the entire data enabled the comparison of DTI and DSI using the same data although this has inherent problems from the standpoint that the diffusion at high levels of diffusion weighting is non-Gaussian. It is interesting that the WM FA from the entire data set was significantly higher than values that are typically measured in most DTI studies. This was because the restricted diffusion measurements in the directions perpendicular to WM tracts exhibited very slow diffusivities, which increased the FA. The MD of WM was also shifted towards lower values. These observations were caused by more apparent restricted diffusion at higher diffusion weighting. An alternative comparison strategy would have been to collect DTI data with an optimized protocol over the same period of time as the HYDI experiment. The latter option was not considered as the acquisition would have been too lengthy compared to most DTI protocols and it is well known that FA is quite heterogeneous in the CNS even with high SNR data.

In the end, what is most critically important is how these measures reflect tissue changes associated with disease processes, thus future studies will need to evaluate these methods in different animal models and disease groups. To date, only a small number of studies have been published regarding the relationships between disease and high diffusion weighting measurements including *q*-space based approaches and fast/slow diffusivity measurements. Several recent studies showed that the *q*-space measurements appeared to be sensitive to both changes associated with normal brain development (Ben Bashat et al., 2005) and disease in multiple sclerosis (Assaf et al., 2002a,b), vascular dementia (Assaf et al., 2002a,b), dysmyelination (Biton et al., 2006), spinal cord injury (Nossin-Manor et al., 2002) and gliosis associated with epilepsy (Eidt et al., 2004). Measurements of fast and slow diffusivity have recently been investigated in prostate and brain tumors (Mulker et al., 2006; Maier et al., 2001, respectively) and stroke (Brugieres et al., 2004). Ultimately, the utility of these new high diffusion weighting approaches like HYDI will depend upon whether they also improve the specificity of tissue pathology.

Several researchers have described methods for characterizing non-Gaussian diffusion including diffusion kurtosis (Jensen et al., 2005; Lu et al., 2006) and stretched exponentials (Bennett et al., 2003, 2004). In this study, non-Gaussian behavior was characterized by using the root-mean-square (RMS) of the residuals from the diffusion tensor fit. This approach was attractive in its simplicity and was similar to the Chi-squared error measure used by Maier et al. (2003) for characterizing tumor pathology. As Figs. 1(d, h) demonstrated, the RMS residuals from the Gaussian fit were greatest in WM, intermediate in GM and dark in CSF. The RMS residual map in Fig. 1(d) was similar to the geometric or arithmetic mean signal images at the highest diffusion weighting (Figs. 1(l) and 3(a, b)) as the simple DT model predicted that the signal will be almost completely attenuated at the highest diffusion weighting. The appearance of the RMS residual map for DT fit to the entire HYDI data was slightly different and also appears more heterogeneous.

For applications, such as white matter tractography, which require the characterization of complex white matter organization (e.g., fiber crossing and orientations), computer simulations showed that the HYDI-QBI appears to provide slightly higher angular resolution than the full HYDI data set. Overall, the ODF profiles from QBI appeared sharper with fewer artifactual side lobes. The angular resolution may be improved by increasing the number of measurements in the outer shell although the relative improvement appeared to be small in a recently published study (Hess et al., 2006).

In this study, the QBI-ODF were calculated using the straight Funk–Radon Transform (Tuch et al., 2003; Tuch, 2004), although recent studies by Hess et al. (2006), Özarslan et al. (2006) and Khachaturian et al. (2007) describe alternative methods that may improve the accuracy of the ODF profiles further. The latter two approaches utilized diffusion measurements at lower diffusion weighting to improve the ODF performances. However, unlike our multiple-shells ODF, a direct radial integration of PDF, which is considered as a linear operation, these approaches used more complicated computation algorithms such as model fitting with assumptions of bi-exponential decay (Özarslan et al., 2006) and nonlinear fusion of spherical Gabor wavelet bases (Khachaturian et al., 2007). The latter study by Khachaturian et al. is consistent with our ODF comparison results between DSI and QBI. They demonstrated that the ODF profiles from QBI appeared sharper than the ODF profiles obtained through a linear combination of QBI and DTI data, which has some similarities to the DSI data used here. However, their nonlinear fusion method did appear to yield sharper ODF profiles. Future studies will investigate the application of more advanced methods for ODF estimation, which should be feasible using HYDI.

The protocol described here may be feasible for research applications with a reasonable scan time (<30 min) for whole brain coverage with 30–50 slices. The overall scan time of this protocol was likely too long for practical use in the clinic. However, targeted studies with fewer slices may be possible in a clinically feasible time (under 10 min). It should be noted that the image data was collected using cardiac gating, which appears to reduce the signal variability and artifacts from pulsatile brain motion (Nunes et al., 2005). Since high *b* values will increase the sensitivity to physiological motion, cardiac gating is recommended. However, shorter scans (i.e., ~30–40% reductions in scan time) may be achieved without gating at the increased risk of local motion artifacts. Future studies may be able to identify the specific *q*-space signal features that are critical for assessment of disease-related changes to tissue microstructure. This strategy may enable the technique to be tailored to general protocols that would be practical in a clinical setting.

One issue related to quantitative diffusion-weighted measurements was the use of signals near the noise “floor”. In DTI, low DW signals cause an underestimation of the signal attenuation, thus the diffusivities will be underestimated (Jones and Basser, 2004). This was likely the case for our diffusion measurements in the outer ($b=6000$ and 9375 s/mm²) shells (Fig. 3 and Tables 5 and 6). These estimates may be improved using Rician noise models for low signals (Koay and Basser, 2006) and this will be investigated further in future studies.

In this study, the *q*-space encoding scheme of HYDI was derived empirically and is not necessarily optimal. Future studies will investigate the effects of different sampling strategies. However, there are several important strategies in designing a

good HYDI scheme. First, the angular sampling on each shell should be as uniform as possible. Second, the number of q -space shells is an important consideration as this will enable the characterization of non-Gaussian diffusion decay. Overall, the HYDI approach is very flexible and the optimum encoding scheme will depend upon the application and the information that is deemed most important. For example, more samples in the outer shells (e.g., improved angular resolution) may be more optimal for characterizing complex WM and white matter tractography studies in regions with crossing white matter tracts. Conversely, in studies that focus on DTI properties, it may be more desirable to obtain more measurements at lower diffusion weighting.

Finally, since HYDI uses non-Cartesian sampling, under-sampling errors will appear differently from Cartesian DSI. In the current HYDI encoding strategy, the sampling density in the radial direction is higher than the angular direction, which may lead to aliasing in the angular direction. The tradeoff between Cartesian DSI and HYDI is the increased flexibility in the DW image analysis methods being used for HYDI. Future studies will need to compare HYDI directly with DSI to establish the relative benefits.

Conclusion

To our knowledge, this study is the first to demonstrate simultaneous measurements of DTI, QBI, DSI and bi-exponential diffusion from a single data set in a moderate scan time on a clinical MRI scanner. The proposed HYDI method is a flexible q -space encoding scheme that may be tailored to emphasize specific diffusion features and is amenable to a wide range of diffusion image analysis strategies. Further investigations are necessary to optimize the HYDI encoding scheme for specific applications. Finally, the approach needs to be evaluated for characterizing clinical pathology relative to diffusion tensor imaging to establish whether the increase in scan time is justified.

Acknowledgments

This work was supported by the National Institute of Mental Health grants: MH62015 and NS050466, and the National Multiple Sclerosis (MS) Society: Translational Research Partnership Grant. The authors would like to thank Pradeep C. Venkat and Alexey A. Samsonov for very helpful discussions.

References

- Alexander, A.L., Hasan, K.M., Lazar, M., Tsuruda, J.S., Parker, D.L., 2001. Analysis of partial volume effects in diffusion-tensor MRI. *Magn. Reson. Med.* 45, 770–780.
- Alexander, D.C., Barker, G.J., Arridge, S.R., 2002. Detection and modeling of non-Gaussian apparent diffusion coefficient profiles in human brain data. *Magn. Reson. Med.* 48, 331–340.
- Assaf, Y., Basser, P.J., 2005. Composite hindered and restricted model of diffusion (CHARMED) MR imaging of the human brain. *NeuroImage* 27, 48–58.
- Assaf, Y., Cohen, Y., 1998a. Non-mono-exponential attenuation of water and *N*-acetyl aspartate signals due to diffusion in brain tissue. *J. Magn. Reson.* 131 (1), 69–85.
- Assaf, Y., Cohen, Y., 1998b. In vivo and in vitro bi-exponential diffusion of *N*-acetyl aspartate (NAA) in rat brain: a potential structural probe? *NMR Biomed.* 11 (2), 67–74.
- Assaf, Y., Cohen, Y., 1999. Structural information in neuronal tissue as revealed by q -space diffusion NMR spectroscopy of metabolites in bovine optic nerve. *NMR Biomed.* 12 (6), 335–344.
- Assaf, Y., Cohen, Y., 2000. Assignment of the water slow-diffusing component in the central nervous system using q -space diffusion MRS: implications for fiber tract imaging. *Magn. Reson. Med.* 43 (2), 191–199.
- Assaf, Y., Mayk, A., Cohen, Y., 2000. Displacement imaging of spinal cord using q -space diffusion-weighted MRI. *Magn. Reson. Med.* 44 (5), 713–722.
- Assaf, Y., Ben-Bashat, D., Chapman, J., Peled, S., Biton, I.E., Kafri, M., Segev, Y., Hendler, T., Korczyn, A.D., Graif, M., Cohen, Y., 2002a. High b -value q -space analyzed diffusion-weighted MRI: application to multiple sclerosis. *Magn. Reson. Med.* 47, 115–126.
- Assaf, Y., Mayzel-Oreg, O., Gigi, A., Ben-Bashat, D., Mordohovitch, M., Verchovsky, R., Reider-Groswasser, I.I., Hendler, T., Graif, M., Cohen, Y., Korczyn, A.D., 2002b. High b value q -space-analyzed diffusion MRI in vascular dementia: a preliminary study. *J. Neurol. Sci.* 203–204, 235–239.
- Assaf, Y., Freidlin, R.Z., Rohde, G.K., Basser, P.J., 2004. New modeling and experimental framework to characterize hindered and restricted water diffusion in brain white matter. *Magn. Reson. Med.* 52 (5), 965–978.
- Barber, C.B., Dopkin, D.P., Huhdanpaa, H.T., 1996. The Quickhull algorithm for convex hulls. *ACM Trans. Math. Softw.* 22 (4), 469–483 (<http://www.acm.org/pubs/citations/journals/toms/1996-22-4/p469-barber/>).
- Basser, P.J., Pierpaoli, C., 1996. Microstructural and physiological features of tissues elucidated by quantitative-diffusion-tensor MRI. *J. Magn. Reson. Med.* 111, 209–219.
- Ben Bashat, D., Ben Sira, L., Graif, M., Pianka, P., Hendler, T., Cohen, Y., Assaf, Y., 2005. Normal white matter development from infancy to adulthood: comparing diffusion tensor and high b value diffusion weighted MR images. *J. Magn. Reson. Imaging* 21, 503–511.
- Bennett, K.M., Schmainda, K.M., Bennett, R., Rowe, D.B., Lu, H., Hyde, J.S., 2003. Characterization of continuously distributed cortical water diffusion rates with a stretched-exponential model. *Magn. Reson. Med.* 50, 727–734.
- Bennett, K.M., Hyde, J.S., Rand, S.D., Bennett, R., Krouwer, H.G.J., Rebro, K.J., Schmainda, K.M., 2004. Intravoxel distribution of DWI decay rates reveals C6 glioma invasion in rat brain. *Magn. Reson. Med.* 52, 994–1004.
- Biton, I.E., Duncan, I.D., Cohen, Y., 2006. High b -value q -space diffusion MRI in myelin-deficient rat spinal cords. *Magn. Reson. Imaging* 24, 161–166.
- Brugieres, P., Thomas, P., Maraval, A., Hosseini, H., Combes, C., Chafiq, A., Ruel, L., Breil, S., Peschanski, M., Gaston, A., 2004. Water diffusion compartmentation at high b values in ischemic human brain. *AJNR Am. Neuroradiol.* 25, 692–698.
- Callaghan, P.T., 1991. Principles of Nuclear Magnetic Resonance Microscopy. Clarendon Press, Oxford.
- Campbell, J.S.W., Siddiqi, K., Pike, B.G., 2004. Full-brain q -ball imaging in a clinically acceptable time: application to white matter fiber tractography. Proc. 12th Annual Meeting ISMRM, Kyoto, Japan.
- Campbell, J.S.W., Siddiqi, K., Rymar, V.V., Sadikot, A.F., Pike, B.G., 2005. Flow-based fiber tracking with diffusion tensor and q -ball data: validation and comparison to principle diffusion direction techniques. *NeuroImage* 27, 725–736.
- Clark, C.A., Le Bihan, D.L., 2000. Water diffusion compartmentation and anisotropy at high b values in the human brain. *Magn. Reson. Med.* 44, 852–859.
- Cook, P.A., Bai, Y., Nedjati-Gilani, S., Seunarine, K.K., Hall, M.G., Parker, G.J., Alexander, D.C., 2006. Camino: open-source diffusion-MRI reconstruction and processing. Proc. 14th Annual Meeting ISMRM, Seattle, WA, USA, p. 2759.
- Cory, D.G., Garroway, A.N., 1990. Measurement of translational displacement probabilities by NMR—An indicator of compartmentation. *Magn. Reson. Med.* 14, 435–444.

- Eidt, S., Kendall, E.J., Obenaus, A., 2004. Neuronal and glial cell populations in the piriform cortex distinguished by using an approximation of q -space imaging after status epilepticus. *AJNR Am. J. Neuroradiol.* 25, 1225–1233.
- Frank, L.R., 2000. Characterization of anisotropy in high angular resolution diffusion-weighted MRI. *Magn. Reson. Med.* 47, 1083–1099.
- Hasan, K.M., Parker, L.D., Alexander, L.A., 2001. Comparison of gradient encoding schemes for diffusion-tensor MRI. *J. Magn. Reson. Imaging* 13, 769–780.
- Hess, C.P., Mukherjee, P., Han, E.T., Xu, D., Vigneron, D.B., 2006. Q -ball reconstruction of multiple fiber orientations using the spherical harmonic basis. *Magn. Reson. Med.* 56, 104–117.
- Inglis, B.A., Bossart, E.L., Buckley, D.L., Wirth III, E.D., Mareci, E.D., 2001. Visualization of neural tissue water compartments using biexponential diffusion tensor MRI. *Magn. Reson. Med.* 45, 580–587.
- Jensen, J.H., Helper, J.A., Ramani, A., Lu, H., Kaczynski, K., 2005. Diffusional kurtosis imaging: the quantification of non-Gaussian water diffusion by means of MRI. *Magn. Reson. Med.* 53, 1432–1440.
- Jones, D.K., Basser, P.J., 2004. Squashing peanuts and smashing pumpkins: how noise distorts diffusion-weighted MR data. *Magn. Reson. Med.* 52, 979–993.
- Khachaturian, M.H., Wisco, J.J., Tuch, D.S., 2007. Boosting the sampling efficiency of q -ball imaging using multiple wavevector fusion. *Magn. Reson. Med.* 57, 289–296.
- King, M.D., Houseman, J., Roussel, S.A., van Bruggen, N., Williams, S.R., Gadian, D.G., 1994. q -Space imaging of the brain. *Magn. Reson. Med.* 32, 707–713.
- King, M.D., Houseman, J., Gadian, D.G., Connelly, A., 1997. Localized q -space imaging of the mouse brain. *Magn. Reson. Med.* 38, 930–937.
- Koay, C.G., Basser, P.J., 2006. Analytically exact correction scheme for signal extraction from noisy magnitude MR signals. *J. Magn. Reson.* 179, 317–322.
- Liu, C., Bammer, R., Acar, B., Moseley, M.E., 2004. Characterizing non-Gaussian diffusion by using generalized diffusion tensor. *Magn. Reson. Med.* 51, 924–937.
- Lu, H., Jensen, J.H., Ramani, A., Helper, J.A., 2006. Three-dimensional characterization of non-Gaussian water diffusion in humans using diffusion kurtosis imaging. *NMR Biomed.* 19, 236–247.
- Maier, S.E., Bogner, P., Bajzik, G., Mamata, H., Mamata, Y., Repa, I., Jolesz, F.A., Mulkern, R.V., 2001. Normal brain and brain tumor: multicomponent apparent diffusion coefficient line scan imaging. *Radiology* 219, 842–849.
- Maier, S.E., Hamata, H., Mulkern, R.V., 2003. Characterization of normal brain and brain tumor pathology by chi-squares parameter maps of diffusion-weighted image data. *Eur. J. Radiol.* 45, 199–207.
- Maier, S.E., Vajapeyam, S., Mamata, H., Westin, C.F., Jolesz, F.A., Mulkern, R.V., 2004. Biexponential diffusion tensor analysis of human brain diffusion data. *Magn. Reson. Med.* 51, 321–330.
- Mulker, R.V., Szot Barnes, A., Haker, S.J., Hung, Y.P., Rybicki, F.J., Maier, S.E., Tempny, C.M.C., 2006. Biexponential characterization of prostate tissue water diffusion decay curves over an extended b -factor range. *Magn. Reson. Imaging* 24, 563–568.
- Mulkern, R.V., Gudbjartsson, H., Westin, C.-F., Zengingonul, H.P., Gartner, W., Guttman, C.R.G., Robertson, R.L., Kyriakos, W., Schwarz, R., Holtzman, D., Jolesz, F.A., Mair, S.E., 1999. Multi-component apparent diffusion coefficients in human brain. *NMR Biomed.* 12, 51–62.
- Niendorf, T., Dijkhuizen, R.M., Norris, D.G., Campagne, M., Nicolay, K., 1996. Biexponential diffusion attenuation in various states of brain tissue: implications for diffusion-weighted imaging. *Magn. Reson. Med.* 36 (6), 847–857.
- Nossin-Manor, R., Duvdevani, R., Cohen, Y., 2002. q -Space high b value diffusion MRI of hemi-crush in rat spinal cord: evidence for spontaneous regeneration. *Magn. Reson. Imaging* 20, 231–241.
- Nunes, R.G., Jezzard, P., Clare, S., 2005. Investigations on the efficiency of cardiac-gated methods for the acquisition of diffusion-weighted images. *J. Magn. Reson.* 177, 102–110.
- Özarslan, E., Mareci, T.H., 2003. Generalized diffusion tensor imaging and analytical relationships between diffusion tensor imaging and high angular resolution diffusion imaging. *Magn. Reson. Med.* 50, 955–965.
- Özarslan, E., Shepherd, T.M., Vemuri, B.C., Blackband, S.J., Mareci, T.H., 2006. Resolution of complex tissue microarchitecture using the diffusion orientation transform (DOT). *NeuroImage* 31, 1086–1103.
- Pierpaoli, C., Basser, P.J., 1996. Toward a quantitative assessment of diffusion anisotropy. *Magn. Reson. Med.* 36, 893–906.
- Ronen, I., Kim, K.H., Garwood, M., Ugurbil, K., Kim, D.S., 2003. Conventional DTI vs. slow and fast diffusion tensors in cat visual cortex. *Magn. Reson. Med.* 49, 785–790.
- Tuch, D.S., 2004. Q -Ball imaging. *Magn. Reson. Med.* 52, 1358–1372.
- Tuch, D.S., Reese, T.G., Wiegell, M.R., Wedeen, V.J., 2003. Diffusion MRI of complex neural architecture. *Neuron* 40, 885–895.
- Wedeen, V.J., Reese, T.G., Tuch, D.S., Weigel, M.R., Dou, J.-G., Weiskoff, R.M., Chessler, D., 2000. Mapping fiber orientation spectra in cerebral white matter with Fourier-transform diffusion MRI. *Proc. of the 8th Annual Meeting of ISMRM*. California.
- Wedeen, V.J., Hagmann, P., Tseng, W.-Y.J., Reese, T.G., Weisskoff, R.M., 2005. Mapping complex tissue architecture with diffusion spectrum magnetic resonance imaging. *Magn. Reson. Med.* 54, 1377–1386.
- Wong, S.T.S., Roos, M.S., 1994. A strategy for sampling on a sphere applied to 3D selective RF pulse design. *Magn. Reson. Med.* 32, 778–784.
- Wu, Y.-C., 2006. Diffusion MRI: tensors and beyond (Doctoral Dissertation). Madison, Wisconsin: University of Wisconsin-Madison. 68–87.
- Wu, Y.-C., Alexander, A.L., 2005a. Hybrid diffusion imaging. *Proc. of the 13th Annual Meeting of ISMRM*, Miami, USA, p. 578.
- Wu, Y.-C., Alexander, A.L., 2005b. Effects of the finite q -space sampling in DSI. *Proc. of the 13th Annual Meeting of ISMRM*, Miami, USA, p. 576.
- Zhang, Y., Brady, M., Smith, S., 2001. Segmentation of brain MR images through a hidden Markov random field model and the expectation-maximization algorithm. *IEEE Trans. Med. Imaging* 20 (1), 45–57.